Modelling the contribution of wind waves to Cap Ferret's updrift erosion

Alphonse Nahon, Déborah Idier, X. Bertin, Thomas Guérin, Vincent Marieu, Nadia Sénéchal, Julie Mugica

Modelling the contribution of wind waves to Cap Ferret's updrift erosion

Alphonse Nahon[1,2,3*], Déborah Idier [4], Xavier Bertin[5], Thomas Guérin [6], Vincent Marieu[1], Nadia Sénéchal[1] and Julie Mugica[7]

Highlights

- Residual sediment transport is modelled at a mixed energy tidal inlet.
- Waves with tides create transport gradients near the inlet's updrift spit extremity.
- Larger or more oblique waves deepen this gradient and reinforce the sand deficit.
- Physically sounded explanation to enhanced spit erosion during NAO+ winters.
- Bed roughness models need to be improved for 2DH inlet-spit morphodynamic modelling.

Keywords

Sandspit; Tidal inlet; Sediment transport; Wave power; NAO; SCHISM.

Modelling the contribution of wind waves to Cap Ferret's updrift erosion

Alphonse Nahon[1,2,3*], Déborah Idier [4], Xavier Bertin[5], Thomas Guérin [6], Vincent Marieu[1], Nadia Sénéchal[1] and Julie Mugica[7]

[1] Université de Bordeaux, UMR CNRS 5805 EPOC, Pessac, France.

[2] BRGM – French Geological Survey, Pessac, France.

[3] National Laboratory for Civil Engineering, Lisbon, Portugal

[4] BRGM – French Geological Survey, Orléans, France.

[5] UMR 7266 LIENSs CNRS-La Rochelle Université, La Rochelle, France.

[6] Benoit Waeles Consultancy in Coastal Engineering (BW-CGC), Brest, France.

[7]BRGM – French Geological Survey, Bastia, France.

* corresponding author, now at National Laboratory for Civil Engineering, Av. do Brasil, 101, 1700-066, Lisbon, Portugal - anahon@lnec.pt

Abstract

Wind waves breaking at an angle with the shoreline force the drifting of littoral sediments, which is known for contributing to the formation and growth of barrier spits. Intriguingly, increased rates of longshore wave power have also been associated with the erosion of some barrier spits on the updrift margin of tidal inlets. Therefore, a numerical experiment was designed and is presented here, which investigates the possible links between the longshore wave power and the shortening of these elongated coastal barriers. Based on a process-based model, this experiment provides new insights into the forces at play in the redistribution of sediments between a sandspit and its adjacent inlet, respectively the Cap Ferret and the Bay of Arcachon's tidal inlet, in SW France. More particularly, model scenarios were defined that show how combined waves and tide create gradients of residual sediment transport responsible for a sediment deficit at the spit – inlet boundary. The deficit was also found to deepen with increasing longshore wave energy, as if the transfer of sediment from the spit to inlet shoals was accelerated. This physically explains the previously observed retreat of the

spit's distal end during periods dominated by the positive phase of North Atlantic Oscillation (NAO) in winter. Indeed, according to model results, higher and/or more oblique waves associated with the positive phase of the NAO are expected to increase the transfer and storage of the drifting sediments to and by the inlet shoals, and this at the expense of the spit. While these conclusions remain valid, we noticed that the sensitivity of model results to the parametrized bottom friction enhanced the importance of accurately representing the spatio-temporal distribution of bed roughness when investigating the morphodynamic interactions between real-world tidal inlets and their margins.

Highlights

- Residual sediment transport is modelled at a mixed energy tidal inlet.
- Waves with tides create transport gradients near the inlet's updrift spit extremity.
- Larger or more oblique waves deepen this gradient and reinforce the sand deficit.
- Physically sounded explanation to enhanced spit erosion during NAO+ winters.
- Bed roughness models need to be improved for 2DH inlet-spit morphodynamic modelling.

Keywords

Sandspit; Tidal inlet; Sediment transport; Wave power; NAO; SCHISM.

1. Introduction

Interactions of sandy and gravelly barriers with tidal inlets play a key role in the behaviour and resilience of coastal barrier systems (Nienhuis and Lorenzo-Trueba, 2019; Oertel, 1985). Empirical theories have long been supporting that the waves work in favour of the barriers, while the tides maintain the inlets open (Davis and FitzGerald, 2004; Hayes, 1979; Nichols and Allen, 1981). More quantitatively, the wave-driven longshore sediment transport (LST) is the main contribution to spit growth in tidal inlet reservoir models (Hoan et al., 2011; Kraus, 2000; Larson et al., 2007). This is also supported by process-based morphodynamic modelling of idealized and migrating tidal inlets (Nienhuis and Ashton, 2016). At the same time, increased longshore wave energy is thought to have contributed to barrier erosion and shortening at the entrance of two mixed-energy barrier systems in Europe. The first example is Skallingen barrier spit, along the Danish North Sea. The distal end of the spit is bounded by a tidal inlet and Aagaard et al. (2004) have reported a shift in the wind regime, between 1970 and 1999, which has increased the rate of wave-driven LST. Aagaard and Sørensen (2013) further quantified this increase as the main contributor to the updrift erosion of the barrier spit's distal end. The second example is Cap Ferret barrier spit. Along the SW Atlantic coast of France, this sandspit dips into the tidal inlet of the Bay of Arcachon. According to a 250-year long geomorphological record, higher and more oblique waves associated with the predominance of the positive phase of the North Atlantic Oscillation (NAO) in winter can trigger the updrift erosion of this sandspit (Nahon et al., 2019). These observations recall that the processes underlying the relationship between LST and the edification of barrier spits could be more subtle than generally assumed. Thus, process-based sediment transport models can help clarifying the role of wave driven LST at the inlet – spit boundary.

Applied to tidal inlets, process-based models have brought a wealth of physically sounded insights into the interaction between waves, tides, and morphology. These models may be fully three dimensional (Bertin et al., 2020) or integrated in the vertical (i.e., 2DH). Nowadays, 2DH models have

66 reached a level of maturity allowing their use to, for instance, investigate the role of non-linear
67 interactions between wave and tidal forces in the redistribution of sediments between the updrift
68 and downdrift margins of tidal inlets (Herrling and Winter, 2018). Also of particular interest for the
69 present study, Bertin et al. (2009) and Hansen et al. (2013) have detailed how barotropic pressure
70 gradients and wave refraction over ebb-tidal shoals affect longshore circulation near tidal inlets, and,
71 in the case of Bertin et al. (2009), how sediment transport is impacted. Before that, Cayocca's
72 pioneer works (2001, 1996) had shown how waves speed up the formation of the (tidal) channel that
73 bounds the Cap Ferret. This importance of waves in the development of tidal channels was recently
74 confirmed by Lenstra et al. (2019). To build on these results, the present study involved a new
75 implementation of a fully coupled circulation, waves, and sediment transport modelling system to
76 the Bay of Arcachon's tidal inlet. To investigate the role that increased longshore wave energy may
77 play in Cap Ferret's updrift erosion, the model was forced using a regional wave hindcast to derive
78 scenarios representative of the local variability of the wave climate at this mixed-energy location.

79 The next section presents in more detail the study area and its wave climate since the second half of
80 the 20th century. Then, section 3 presents the implementation of the modelling system as well as the
81 simulation scenarios, and further describes how the modelled sediment transport was processed and
82 analysed. In section 4, model results are presented in terms of residual longshore sediment transport
83 and sedimentation patterns. This leads to the subsequent discussion of the role of waves and wave
84 climate variability in the erosion of barrier spit bounded by tidal inlets. The question of the
85 parameterization of bottom friction is also discussed as it appeared to largely influence the rates of
86 sediment exchange between the spit and the inlet shoals.

87 ## 2. Study area and local wave climate

88 ### *2.1. Study area*

89 The barrier system of the Bay of Arcachon (**Figure 1**) lies in the highly infilled incised-valley segment
90 of the Leyre river's estuary (Allard et al., 2009; Féniès and Lericolais, 2005). On the updrift margin of

91 the estuary, NW dominant waves generate an estimated 661 x 10^3 m^3 net annual littoral drift (Idier et
92 al., 2013). Southward drifting littoral sediments have progressively edified the Cap Ferret sandy spit
93 which now semi-encloses a mesotidal lagoon and dips into a tidal inlet exposed to a mixed-energy
94 environment (annual mean significant wave height of 1.68 m and mean spring tidal range of 3.80 m;
95 Nahon, 2018). According to navigation charts, the inlet has stopped its southward migration around
96 1900 (Nahon, 2018). Nonetheless, channels and bars continue to swept the inlet ebb-tidal delta in
97 the downdrift –north to south— direction (Capo et al., 2014; Cayocca, 2001). This sustained
98 southward displacement contrasts with the large scale north-south oscillations the distal end of the
99 spit has displayed over the last 250 years (Nahon, 2018). So, the spit has eroded updrift at some
100 point, and the last updrift erosion (**Figure 1**, lower panels) began as the longshore wave power
101 sharply increased in the early 1970s (**Figure 2**, upper panel). In the same time, the enlargement of
102 the adjacent inlet only began after 1980 (Nahon, 2018). This enlargement of the inlet could be the
103 results of an increasing tidal prism, driven by higher rates of SLR, which also leads to larger
104 equilibrium volumes of the inlet's flood- and ebb-tidal deltas (Walton and Adams, 1976). Therefore,
105 it was hypothesized that the spit oscillations were a combined response to the variations of the
106 longshore wave power, associated with the phase (negative or positive) of the North Atlantic
107 Oscillation (NAO; Hurrell & Deser, 2009), and to the variations in the rate of SLR (Nahon et al., 2019).

108 *2.2. Wave hindcast*

109 Across the last spit-end oscillation (**Figure 1**, lower panels), the local wave climate was hindcasted
110 (from 1949 to 2014) using the storm surge modelling system of Bertin et al. (2015). The model was
111 extended to the whole North Atlantic Ocean as described in Arnoux et al. (2018) and was forced with
112 wind fields originating from the NCEP/NCAR reanalysis (Kalnay et al., 1996). Modelled wave
113 parameters were previously validated against directional wave buoy measurements. **Figure 3** shows
114 the model – data comparison in terms of longshore wave power, and the position of the wave buoy,
115 15 km offshore of the Cap Ferret and in 54 m water depth, is indicated in **Figure 4** (left panel, W).

Using a total of 5.3 years of record between 2007 and 2014, Nahon et al. (2019) indicated that the averaged wave power (WP) and the longshore wave power (WPy) were underestimated by 2.4% and 1.7% respectively. Also, at the observation sampling frequency (i.e., one observation every 30 min), linear correlation coefficients between modelled and measured values were of 0.93 and 0.81 for WP and WPy. When considering 90-day running mean of WP and WPy, these coefficients grow to 0.99 and 0.95, respectively.

Following Charles et al. (2012), this hindcast was used to further highlight the apparent relationship between the North Atlantic Oscillation (NAO) and the local wave climate in winter (December to March; DJFM). During the positive phase of the NAO, the significant wave height (Hs) increases, and the mean direction of wave incidence deviates clockwise from shore normal. As a result, winter averaged WPy is positively correlated with the NAO index. To illustrate this correlation, upper panel on **Figure 2** shows the decadal average of the winter NAO index (station-based index; Hurrell, 2015) and of the winter WPy since 1950. From winter 1950 to winter 1972, the decreasing trend in the decentred average of the winter NAO index indicates the negative phase of the NAO has prevailed. By opposition, the positive phase has dominated from 1972 to mid-1990s, as revealed by the ascending trend of the averaged index. Also, over the period 1950-1972, the average of winter WPy was equal to 89.27 % of its 1950-2014 average value, when over 1973-1995 it reaches 112.49 % of it. Those two 23-year periods respectively cover the last phase of Cap Ferret elongation (1950-1972) and the onset of the rapid spit retreat around 1972-1973. Therefore, average WPy over these periods were used to derive different scenarios to force the sediment transport model, which are presented in section 3.2.

3. Modelling methodology

3.1. Model implementation and validation

The modelling system SCHISM (Zhang et al., 2016) was used to simulate hydrodynamics and sediment transport around the spit distal end. **Figure 4** shows the computational domain and the

model bathymetry. SCHISM's circulation model was used in 2DH mode, fully coupled to the spectral wave model WWM-II (Roland et al., 2012). Both models' equations are solved over the same unstructured grid; they were run in parallel and used the same domain decomposition. The grid resolution ranges from 2 km at the open boundary to 60 m within the inlet and lagoon; along the last 6 km of spit's ocean side, the resolution reaches 20 m which is expected to be fine enough to generate wave induced circulation at this type of beaches (e.g., Bruneau et al., 2014, used a 15 m resolution grid at the nearby Biscarosse Beach for waves less than half the size of those in the present study).

In WWM-II, the wave energy spectra was discretized over a 24 x 24 grid, spanning directions from 0° to 360° and frequencies from 0.04 Hz to 0.4 Hz; wave breaking was parameterized according to Battjes and Janssen (1978), with a breaking criteria equal to 0.78. The hydrodynamic timestep was set to 1 min and the sediment transport fluxes were computed with Camenen & Larson (2007; Larson et al., 2011) formula developed for tidal inlet applications. A relevant characteristic of this formula is to account for the wave and current colinear interactions. To do so, bedload and suspended load transport rates in the wave propagation direction are respectively computed with the "net sediment transporting velocity" and the "net mean current" (Camenen and Larson, 2007; equations 226, 227 and 231 for bedload and equations 232 and 241 for suspended load). Both quantities are deduced from the root-mean-square total of the velocity over a wave period. This total velocity is defined as the wave orbital velocity plus the component of the ambient current aligned with the wave propagation direction. As a result, if waves and current are not perpendicular, waves add to the net transport (either onshore or offshore) in the direction of wave propagation. This, independently of the asymmetric character of the waves which was not considered here.

In the circulation model, the bottom friction was parametrized with a Manning formulation. To avoid the modulation of modelled sediment transport patterns by a spatially varying Manning coefficient, the choice was made to use a spatially uniform coefficient, equal to 0.032 $s/m^{1/3}$. This value falls

166 within the range of values found in the literature for tidal inlets (Bruneau et al., 2011; Orescanin et
167 al., 2016) and was set after calibration tests performed with tidal forcing only. For the tests, the
168 model's open boundary was forced with 16 tidal components from the regional tide model of Bertin
169 et al. (2012). The model's performances were evaluated in terms of modelled elevation at three
170 locations across the tidal inlet (**Figure 4**, A, B and C), compared with observations from June 2014.
171 From the west to the east, these observations include: a 28-day long record from a bottom moored
172 pressure sensor located on the terminal lobe of the ebb-tidal delta (A; Senechal et al., 2013), a 14.8-
173 day record from a bottom moored pressure sensor located within the inlet Southern channel (B;
174 Doré, 2015) and a 28-day extraction from *Eyrac*'s tide gauge record (C; SHOM). Root mean square
175 errors of modelled elevation ranged from 7.35 cm at the inlet entrance to 11.84 cm in the lagoon
176 with biases on the order of a few centimetres. These values are summarized in **Table 1** with
177 additional details on the evolution M2 and M4 tidal components across the inlet. The evolution of
178 these components suggests the model qualitatively reproduces the propagation of the tidal wave
179 across the inlet, although tidal asymmetry and distortion may be overestimated locally as the
180 comparison at location B reveals.

181 *3.2. Output processing*

182 The model was then used to assess the impacts of waves and of winter wave climate variability on
183 the residual sediment transport near the distal end of the spit. This was carried on with tidal forcing
184 reduced to a monochromatic tide, represented only with local M2 component imposed along the
185 model's open boundary. The tidal amplitude was set following Cayocca (2001, 1996) who found that
186 residual sediment transport patterns are better approached with a single M2 constituent of
187 amplitude 1.8 m (i.e., 3.6 m tidal range). After a one-day simulation spin up, sediment fluxes sampled
188 at 10-min intervals were averaged over 2 tidal cycles and converted into annual rates of residual
189 sediment transport. Residual fluxes were then interpolated onto a regular grid with a thinner
190 resolution than the unstructured grid. This regular grid served to compute the divergence of the

191 residual fluxes and the divergence was spatially integrated to estimate the annual sedimentation
192 rates over an array of 58 alongshore-overlapping cells (**Figure 5**, centre panel). Each cell is 300-meter
193 wide in the north-south direction. In this same direction, centres of two neighbouring cells are
194 spaced by 100 m which creates a 67% overlap between cells. To discuss the integrated sedimentation
195 rate, the average southward sediment transport was computed for each cell. This quantity was
196 calculated by integrating in the west-east direction the north-to-south component of the residual
197 transport and then averaging of the integrated values over the north-south extension of each cell.

198 Three groups of cells were defined and are delimited on **Figure 5** centre panel: a first group away
199 from the inlet (dashed black frame, delimiting cells number 5 to 10), a second group on the western
200 face of the spit's last kilometre (dashed red frame, delimiting cells number 45 to 53, hereafter
201 referred to as the western group) and a last group at the aerial spit – inlet boundary (dashed blue
202 frame, delimiting cells number 55 to 57, hereafter referred to as southern group). Western and
203 southern groups overlap by 100 m in the north-south direction and were used to present and discuss
204 the modelled patterns of residual sediment transport and sedimentation rates along the last
205 kilometre of the subaerial portion of the spit.

206 To give a broader perspective on the sediment budget, the sedimentation rate over the spit's
207 subtidal platform was also estimated for simulations with both waves and tide (SIM3-8, see section
208 2.5). As for the array of cells, the annual sedimentation rate was computed by integrating the
209 divergence of the sediment fluxes. The right panel in **Figure 4** shows the area (delimited in blue) over
210 which the spit-platform sedimentation rate was computed. This area overlaps with the array of cells
211 after cell number 39. Furthermore, the sedimentation rate is integrated only in zones shallower than
212 -7 m NGF which distinguishes inlet shoals and channels (black contour on **Figure 4**, right panel).

213 *3.3. Simulation scenarios*

214 Residual transport rates and sedimentation estimations were computed for a first set of 3
215 simulations that uncovered the respective and combined roles of waves and tide; the model was run

with M2 tide forcing only (SIM1), with waves and no tides (SIM2) and then with waves and M2 tide (SIM3). A second set of 5 simulations were run to assess the sensitivity of model results to changes in the winter wave climate described in the section 2.2. **Table 2** summarizes wave climate parameters for the 8 simulations.

In SIM1 and SIM3 parameters were representative of the annual average wave power hindcasted between 1949 and 2014. The wave direction (Dir) was the one of the average incoming wave power; the wave peak period (Tp) and the significant wave height (Hs) were the average values (over 1949-2014) multiplied by $\alpha = 1.095$ and $\beta = 1.095^2$, respectively. These coefficients were defined as in Eq. 1 to Eq. 5, where representative significant wave height ($H_{s,rep}$) and peak period ($T_{p,rep}$) are defined so that, along the model's open boundary, the representative wave energy (E_{rep}) and the representative group velocity ($c_{g,rep}$) match the average wave power $\overline{WP}$ over a given period of time T:

$$\overline{WP} = \frac{1}{T}\int_0^T WP(t)\,dt \qquad \text{Eq. 1}$$

$$\overline{WP} = E_{rep}\, c_{g,rep} \qquad \text{Eq. 2}$$

$c_{g,rep}$, computed with $T_{p,rep} = \alpha\, \overline{T_p}$ Eq. 3

$$E_{rep} = \frac{1}{8} g \rho {H_{s,rep}}^2 \qquad \text{Eq. 4}$$

$H_{s,rep} = \beta\, \overline{H_s}$, with $\beta = \alpha^2$ Eq. 5

Winter wave climates were defined in similar fashion, with December to March averages instead of annual averages. SIM4 was representative of all 65 complete winters between December 1949 and March 2014, SIM5 was representative of the low energy winters between 1950 and 1972, and finally SIM6 is representative of the high energy winters between 1973 and 1995. The last two simulations (SIM7 and SIM8) were set to further infer on the role of the wave angle of incidence. As depicted by

Figure 2's lower panel, higher values of winter NAO indices shift clockwise the incoming wave mean direction, producing higher wave angle of incidence. SIM7 and SIM8 were set up with ± 4° shifted Dir to mimic this influence of negative and positive phases of the NAO.

Additionally, tests were made to evaluate the impact of tidal range (**Table 3**). To this end, simulations SIM4 to SIM8 were reproduced with tidal ranges of 1.8 m and 4.5 m (**Table 3**); 1.8 m corresponding to the mean neap tidal range at the entrance of the Bay and 4.5 m being greater than the mean spring tidal range (of 3.8 m) but smaller than the maximum astronomical tidal range of 4.9 m (SHOM, 2014). Later in the discussion, results from four ultimate simulations (SIM3a,b,c and d; **Table 3**) will be presented, that highlights the limits of the current models of spatio-temporally variable bed roughness, at least for the present inlet – spit morphodynamic interactions.

4. Results

4.1. Waves, tides, and residual sediment transport

Figure 6 shows the modelled sediment transport and sedimentation patterns along the last 6 km of the subaerial sandspit. In terms of residual sand transport (upper panel), the southward component of the transport denotes that the LST was insignificant until along the spit's last kilometre in the tide-only case (SIM1, grey curve). Then, away from the spit-end (cells > 55) the southward component became almost equal to that of the wave induced transport (SIM2, red curve). When waves were the only forcing, the updrift, or incoming, rate LST was in the order of 150 x 10^3 m^3/year and the southward transport steadily increased with the curvature of the spit. The transport peaked within the western group of cells (in cell number 51) before it was halved in the southern group. Finally, when both average waves and M2 tide forced the circulation (SIM3, blue curve), the residual southward transport mimicked that of the wave-only simulation until cell number 50 and then increased to be multiplied by a factor of two in cell number 58.

257 The sedimentation rates associated with those transport patterns were then estimated by
258 integrating the divergence of the residual sediment transport (middle panel, **Figure 6**). With tidal
259 forcing only, little sediment accretes or erodes before the very end of the spit, and the average
260 accretion was of 6 x 10^3 m^3/year per cell in the western group (**Table 2**). In the wave-only case, this
261 value grew to 186 x 10^3 m^3/year per cell. Contrastingly, combined average waves with the
262 representative M2 tide produced an erosion of 51 x 10^3 m^3/year per cell on average. Sedimentation
263 rates were less contrasted in the southern group. There, in all three cases, erosion was predicted
264 immediately after the spit extremity. Still, the estimated erosion was much smaller and would
265 happen in a narrower area in SM1 and SIM2 compared to SIM3. Indeed, with combined waves and
266 tide the estimated erosion in the southern group was of 312 x 10^3 m^3/year per cell on average,
267 compared to 95 x 10^3 m^3/year, in the wave-only case.

268 When both waves and tide were considered SIM3, the lower panel in **Figure 6** further displays
269 alongside the contribution of the southward (NS) component and of the eastward (WE) component
270 of the sediment transport to the overall sedimentation rates. It indicates the southward transport
271 would generate mostly erosion (filled-in blue bars), as for instance in the southern group. By
272 opposition, the eastward transport would promote accretion, which mostly fails to compensate the
273 erosion produced by the gradients in the southward transport (red bars).

274 Lastly, the black curve on the upper panel of **Figure 6** also shows the southward residual sediment
275 transport in the case of average winter waves, combined with the representative M2 tide (SIM4).
276 Compared to SIM3, the incoming rate of LST was multiplied by a factor 1.83 (**Table 2**). Then, the
277 southward transport's curve presents a similar shape which denotes a similar acceleration of the
278 transport. Still, the overall acceleration was less pronounced as the increase at the spit – inlet
279 boundary was only about a factor of 1.25 compared to SIM3 (in cell number 58). In the same time,
280 the estimated erosion was reduced in the western group and reinforced in the southern group
281 (**Figure 7**, middle panel, black bars).

4.2. Winter wave climate and tidal range modulations

Figure 7 shows how the estimated sedimentation rates varied within the simulations for the different winter wave climates, and Table 2 summarizes the values of the rate of incoming LST in those simulations. As, the wave direction and the significant wave height varied, according to the hindcasted local wave climate (see section 2.2), the rate LST ranged from 205.0 x 10^3 m^3/year in SIM7 to 411.1 x 10^3 m^3/year in SIM8 (**Table 2**). This corresponds respectively to 1.23 times and 2.47 times the rate in SIM3. As the tidal range was also changed according to its local variations, those rates slightly decreased and increased for smaller and greater M2 tidal amplitudes, respectively (**Table 3**).

In the five simulations with the representative tidal range (middle panel, SIM4 to SIM8), the erosion estimated from the divergence of the residual transport in the southern group increased when the rate of incoming LST also increased. This was the case either with higher or more oblique waves. For instance, from SIM7 to SIM8 the average erosion rate per cell grows by 36 x 10^3 m^3/year. This corresponds to about 10.1 % of the average erosion rate for this area in simulation SIM4. At the same time, from SIM5 to SIM6 the increase was limited to 2.1 %. By opposition, in the simulation with greater values of LST, the erosion in the western group was contained, even with some accretion estimated in SIM6 and SIM8. At the greater scale of the spit platform, positive sedimentation rates prevailed independently of the wave climate. In the case of average winter wave climate (SIM4), the sedimentation rate over the platform was estimated to +704.6 x 10^3 m^3/year, which was modulated by -8% and +16% as the wave direction was shifted by -4° (SIM7, less oblique) and +4° (SIM8, more oblique) respectively (**Table 2**).

Simulations SIM4, 7 and 8, were further reproduced with mean neap and high spring tidal ranges (upper and lower panels on **Figure 7** respectively). Similar to the wave only simulation (SIM2), accretion was predicted in the western group during neap tides. This accretion increased when the wave climate was rotated clockwise and the rate of incoming LST more than multiplied by a factor of two (**Table 3**, SIM7a to SIM8a). Compared to simulations with a representative tidal range, lower

erosion rates were estimated in the southern group. Still, this erosion grew from SIM7a to SIM8a as it did from SIM7 to SIM8. This behaviour was also observed with a greater tidal range (lower panel). So, the erosion driven by the divergence of the residual sediment transport at the spit – inlet boundary (i.e., in the southern group) has increased with incoming rate of LST, and this throughout the entire neap tide – spring tide cycle.

4.3. Contribution of the southward transport

As shown first for SIM3 (**Figure 6**, lower panel), the contribution of the gradient of the southward (NS) to the divergence of total residual transport was calculated for all simulations. **Figure 8** shows the comparison of both integrated quantities in cells number 45 to number 58. For the twelve simulations, two patterns emerged from the Pearson's linear correlation coefficients (upper panel). First, little to no correlation existed between the two quantities in the cases with only tide or only waves. The scatter plot of the sedimentation rates by the NS sedimentation rates (lower left panel on **Figure 8**) further confirm this as the point clouds for SIM1 and SIM2 are dispersed. By opposition, the point cloud for SIM3 confirms the dominant contribution of NS sedimentation rates to the total sedimentation rate, those quantities also displaying a correlation coefficient greater than 0.9. Secondly, the relationship between those two quantities grew either when the tidal range or the longshore wave power increases. This is well visible from SIM4a to SIM4b, where the correlation coefficient grew from 0.56 to 0.93 when the tidal range went from 1.8 m to 4.5 m, and from SIM7a to SIM8a, where the correlation coefficient grew from 0.44 to 0.67 when the wave angle of incidence was shifted 8° clockwise and the incoming LST multiplied by a factor of 2.14. Then, the scatter plots for simulations with winter-representative wave climates (lower right panel on **Figure 8**) confirm that the southward component of the residual sediment transport had a dominant contribution in the cells with maximum erosion.

5. Discussion

5.1. Updrift erosion by waves and tide

The twelve morphostatic simulations (i.e., without morphological evolution) spanned a substantial range of forcing and modelling choices. Those with forcing parameters representative of yearly average waves or tide conditions first revealed that it takes both waves and tide to cause erosion near the subaerial spit terminus (i.e., in SIM3). The normalized sedimentation rates shown on **Figure 9** illustrate this, with waves or tide alone resulting in accretion along the ocean flank of the spit (i.e. in the western group, ΔVw) and causing little to hardly any erosion at the spit edge bounded by the inlet (i.e., in the southern group, ΔVs). By opposition, erosion was predicted in both regions with combined forcings. Furthermore, the simulations with wave parameters representative of average winter conditions indicated these patterns were preserved in winter (SIM4), although with less erosion along the spit flank (**Figure 9**, left table). Also, simulations SIM4a and SIM4b indicated the erosion at the spit edge was a permanent feature throughout the entire neap-spring tidal cycle (**Figure 7**).

These first results are coherent with morphodynamic simulations of Lenstra et al. (2019) and of Cayocca (2001, 1996). Indeed, in the case of Lenstra et al. (2019) it was the combination of waves and tides that caused the breaching and the deepening of new channels near the updrift spit of their idealized tidal inlet. Then, before this, simulations of Cayocca (2001, 1996) for the present real-world inlet had suggested the breaching of new secondary channels across Cap Ferret's spit-platform occurred faster with both forcings, as shown in **Figure 10**. The figure shows the initial bathymetry and the simulated inlet morphology after 50 morphological timesteps, in the case with tidal forcing only (center panel) and in the case with both tidal and wave forcing (right panel). In the latter case, the newly breached secondary channel is deeper in the alignment of the spit and is slightly more bended clockwise. The addition of waves also leads to greater accretion on the beach along the spit's ocean side and on the intertidal shoals of the spit platform. In the present simulations, the sole computation of sediment transport fluxes further revealed which components of the sediment transport could explain this behaviour.

The southward component of the sediment transport produced negative sedimentation rates and appeared to promote the erosion of the spit (**Figure 6**, lower panel). Perpendicular to this, the transport was directed eastward (not shown) and produced positive sedimentation rates. This could be mostly explained by the bulldozer effect of waves at the vicinity of the inlet as described by Bertin et al. (2009), although the colinear wave and current interactions (Camenen & Larson, 2007; as described in sub-section 3.1) may also contribute. Going back to Cayocca's modelled morphology under waves and tide (**Figure 10**, right panel), the acceleration of the southward sediment transport would explain the erosion at the spit edge and the deepening of the channel, and the eastward sediment transport would explain the bending of the channel and the accretion along the flank of the spit.

Therefore, when the acceleration of the sediment transport along the coast (i.e., southward) tears off more sediments than the transport towards the coast (i.e., eastward) brings in, the Cap Ferret erodes and retreats. The sediment budget of the spit then appears to be linked to the balance between these two contributions, and the simulated scenarios indicate this balance was affected on the rate of sediment transport along the coast (**Figure 8**). The sensitivity tests of this balance to the wave climate and to the modelling choices further came to discuss the apparent relationship of the spit behaviour with the winter phase of the NAO and to discuss the apparent limitations of the present numerical experiment.

5.2. Influence of shifting atmospheric circulations

The sensitivity tests to the wave climate aimed to investigate the possible relationships between the updrift erosion of barrier spits and the increase of longshore wave power and/or sediment transport. In agreement with the observations described by Nahon et al. (2019), every time the longshore wave power and the incoming (or updrift) longshore sediment transport either increased or decreased, the erosion at the spit edge (i.e., in the southern group) also increased or decreased respectively (LST and ΔVs values in **Table 2**). These variations remained within a modest +/- 5% range centred on the

382 average winter estimates (**Figure 9**). However, they are fully coherent with the observed relationship
383 between Cap Ferret's behaviour and the variations of the longshore wave power associated with
384 decadal trends of the winter phase of the NAO. Indeed, higher and/or more oblique waves
385 associated with NAO positive winters (**Figure 2**) would cause more erosion at the edge of the spit and
386 this pattern prevailed from neap to spring tidal range (**Figure 7**). Alongside the geomorphological
387 record at Cap Ferret, this brings a physically sounded explanation to the links between the updrift
388 erosion of this barrier spit and the changes of nearshore wave climate caused by a shifting
389 atmospheric circulation. Such relationship was also reported for the Skallingen spit by Aagaard and
390 Sørensen (2013) and it is expected that similar processes may be at play at other places. For instance,
391 on the Pacific coast of Northern America, the updrift (southern) margin of the entrance to Willapa
392 Bay was remarkably eroded during the 2009-2010 El Niño, which had caused the increase of the
393 southerly longshore wave power (Long Beach, in Barnard et al., 2011). Also, along the Dutch North
394 Sea shores, the western margin of Ameland inlet is eroding updrift since 1974 (Elias et al., 2019). At
395 both these locations, the causes to the observed erosion remain to be explicitly stated and the
396 present results may well provide new insights into the forces at play.

397 5.3. From barriers to shoals

398 The sensitivity tests also revealed the accretion rates above the spit platform increased with higher
399 longshore wave power and sediment transport (**Table 2**). Then, the capacity of the spit platform to
400 retain sediment increases, likely due to the role that waves play in the formation of inlet shoals
401 (Ridderinkhof et al., 2016). Also, the predicted positive sedimentation rates are coherent with
402 satellite observations of Capo et al. (2014), who documented the accretion of the spit platform
403 between 1986 and 2012. Therefore, both model results and observations suggest the Cap Ferret
404 subaerial spit erodes at the benefit of its subtidal platform, like in Meistrell's (1972) spit-platform
405 concept in which the subaerial spit release sediments to its platform until this latter one has reached
406 a vertical equilibrium. In this process, the energy brought in by the waves to create this transfer also

increases the capacity of the adjacent platform and shoals to fix the material eroded from the barrier spit. This leads to the hypothesis that increased wave energy may accelerate the release of sediments stored in coastal barriers to the subtidal shoals of tidal inlets, for instance when those are expending due to sea level rise. This would become even more relevant for establishing morphodynamic prediction of barrier systems along shores where the longshore sediment transport presents a climatically-driven variability (Almar et al., 2015; Anderson et al., 2018; Marchesiello et al., 2020; Poirier et al., 2017; Silva et al., 2020; Splinter et al., 2012; Wiggins et al., 2020). Another fundamental aspect for such morphodynamic predictions was found to be the reliance of the results on the bottom friction parameterization.

5.4. Friction parameterization as a major limitation

The adopted morphostatic approach aimed to identify the dominant sediment transport mechanism at the distal end of Cap Ferret. An unexpected behaviour in simulations with both tide and waves was that the model never predicted the retention of sand near the spit-end. This, even when the model was forced with waves representative of the period 1950 –1972, during which aerial photographs documented its growth (**Figure 1**). In fact, according to earlier and recent morphodynamic simulations referred above, this may not be completely surprising. Indeed, like it was reported by van Ormondt et al. (2020), 2DH models may struggle to reproduce the growth of real-world spits near tidal inlets. Some aspects certainly lie in the simplified wave-current interactions in these type of model and would only be overcome with fully coupled 3D models (Bertin et al., 2020). Other aspects may instead be related to the modelling choices and have motivated the further testing of three parameterizations of the spatio-temporal variability of the bed roughness in the circulation model. Indeed, near the spit-end, large-scale bedforms (Vaucher et al., 2018) attest of the spatial variability and the increase of the bottom roughness towards the inlet. Nearly absent along the northern beaches, these bedforms results from the erratic interactions between the waves and the strong ebb- and (dominant) flood-tidal currents. On the intertidal beach,

these bedforms have wavelength of more than a meter, for a height in the order of 30 cm (Vaucher et al. 2018). As a result, they are not resolved by the unstructured grid and need to be parameterized. Brakenhoff et al. (2020) recently reviewed the different approaches to represent the bed friction in these environments, and how modelled sediment transport rates were sensitive to its parameterization. So, simulation SIM3 was reproduce with four different parameterization of the bottom friction (**Table 3**, SIM3a-d).

In the case of a reduced Manning coefficient (0.02 $s/m^{1/3}$, SIM3a), more representative of open beaches (Smith et al., 1993), although the incoming rate of LST was increased by a factor of 2.3 compared to SIM3, the erosion patterns in the southern group were multiplied by a factor in the order of two (**Figure 11**). Then, two bedform predictors were tested as they are a way to estimate the spatio-temporal variability of the bed roughness length. In SIM3b and SIM3c (**Table 3**) the bedform predictors from Soulsby (1997) and van Rijn (2007) were respectively tested, using a log law formula to compute the drag coefficient. In the former case, the predictor returns the maximum value between the skin friction and the sand wave roughness plus the roughness of the current- or wave-generated ripple, in the latter case the predictor returns the skin friction plus the roughness of wave and current ripple roughness, mega-ripple and dunes. **Figure 11** presents the results of those simulations. In the case of Soulsby's (1997) predictor, in black, the results mimicked those obtained with Manning coefficient scaled to reproduce the tidal distortion through the inlet (SIM3, in blue), but which is also expected to overestimate the friction on the updrift open beaches. By opposition, results with van Rijn's (2007) predictor (SIM3c) were very similar those with a Manning coefficient representative of an open beach (SIM3a). Therefore, these predictors produced similar results to spatially constant Manning coefficients and, in the present case, *a priori* failed to represent the expected larger spatial variability. As a result, the model could only be expected to overestimate the erosion of the spit, in one case because the littoral drift would not bring in enough sand, in the other because the transiting sand would not be slowed down sufficiently.

Therefore, an alternative was to use a spatially varying Manning coefficient (like for instance in Bertin et al., 2009; Bruneau et al., 2011; Elias and Hansen, 2013; Teske, 2013), with lower values of the Manning coefficient for the open beaches than for the inlet and lagoon areas. The inset on **Figure 11** presents the spatial repartition of the Manning coefficient, which was derived after Mugica et al. (2016) and empirically based on sediment characteristics and vegetation cover. This reparation led to increased values of the updrift LST while the acceleration of this transport remained relatively limited towards the inlet (SIM3d). As a result, the predicted deficit at the spit-end was reduced, although most significantly within the western group.

These tests highlight how crucial it is to finely tune the bed friction to model spit – inlet morphodynamic interactions, in the present case and highly likely for other real (by opposition to synthetic) tidal inlet morphologies. Although some improvements of the bed roughness predictors (Elias et al., 2015) or the use of anisotropic Manning coefficient should be further tested (Demissie and Bacopoulos, 2017), such tuning appeared possible using a spatially varying Manning coefficient. However, such an approach should be supported/validated by measured elevations and/or velocities data much closer from the spit-end. Here, the spatial distribution was shown to give similar performances, than the calibrated (0.032 $m^{1/3}$.s) Manning coefficient, although this was down with elevation data collected too far away from the area of interest. So, to build a realistic 2DH morphodynamic model of the Cap Ferret barrier spit, the next step would be to acquire the missing hydrodynamic data for validating the chosen parameterization of the bed friction.

6. Conclusions

A numerical experiment was performed to investigate the physical processes behind the apparent relationship between the Cap Ferret's updrift erosion and increasing rates of the longshore wave power. Residual sediment transport patterns near the spit-end were simulated with a 2DH process-based model, for a series of twenty morphostatic scenarios of forcing and parameterized bottom friction. Simulations confirmed that waves were contributing to the over-deepening of the secondary

tidal channel bounding the spit, they also suggested it was the acceleration of the longshore component of the sediment transport that was responsible for this over-deepening. This acceleration appeared to create a sediment deficit at the spit – inlet boundary which was found to increase with the wave power. So, the leading hypothesis was confirmed as higher and/or more oblique waves during NOA positive winters would favour the northward (updrift) retreat of the spit-end. By opposition, the cross-shore component was found to promote accretion, although the erosion induced by the longshore component dominated along the western southern flanks of the spit-end. Beyond the spit's bounding channel, accretion became dominant. Indeed, the sedimentation rates above the spit platform were always positive and increased with the wave power. In agreement with previous observations, the erosion of the spit therefore appeared to benefit to the spit-platform. Model results further support this transfer of sediment form the barrier to the shoals was accelerated under increased longshore wave power. However, the modelled transfer was found to be extremely sensitive to the parameterized bottom friction. Possibly because of this, the model failed to predict any positive sediment budget near the spit-end. Indeed, it is suspected the bottom was either too rough to generate a realistic amount of littoral drift, or too smooth to allow the fixation of the drifting sand near the spit end. A finely tuned spatially varying Manning coefficient could be a solution and would require an appropriate hydrodynamic dataset. Finally, the processes and limitations highlighted here are expected to be valid near other barrier spit with similar behaviour. In those places, greater attention should be given to the parameterization of the bottom friction in the morphodynamic modelling of spit – inlet interaction. Especially when inlets are expending at the expense of the spits.

CRediT authorship contribution statement

Alphonse Nahon: Conceptualization, Methodology, Formal analysis, Writing - Original Draft Writing**;** **Déborah Idier:** Methodology, Resources, Writing - Review & Editing**; Xavier Bertin:** Resources, Writing - Review & Editing; **Thomas Guérin:** Resources, Writing - Review & Editing**; Vincent Marieu:** Resources**; Nadia Sénéchal:** Supervision, Writing - Review & Editing; **Julie Mugica:** Supervision, Project administration, Funding acquisition.

Declaration of competing interest

The authors declare that they have no known competing financial interests or personal relationships that could have appeared to influence the work reported in this paper.

Funding

The work was part of a PhD grant co-funded by the BRGM, the Conseil Régional de Nouvelle-Aquitaine and the Syndicat Intercommunal du Bassin d'Arcachon, and part of the project MOSAIC.pt funded by the Portuguese Fundação para a Ciência e Tecnologia (FCT; PTDC/CTA-AMB/28909/2017). Numerical simulations relied on the Avakas computational facility, made available by the Région Nouvelle-Aquitaine, and used resources of the Portuguese National Distributed Computing Infrastructure (INCD) funded by Lisboa2020 Operational Program through the INCD project (LISBOA-01-0145-FEDER-022153).

Acknowledgement

The authors would like to thank Joseph Zhang for making the numerical model SCHISM available.

References

Aagaard, T., Nielsen, J., Jensen, S.G., Friderichsen, J., 2004. Longshore sediment transport and coastal erosion at Skallingen, Denmark. Geografisk Tidsskrift-Danish Journal of Geography 104, 5–14. https://doi.org/10.1080/00167223.2004.10649499

Aagaard, T., Sørensen, P., 2013. Sea level rise and the sediment budget of an eroding barrier on the Danish North Sea coast. Journal of Coastal Research 65, 434–439. https://doi.org/10.2112/SI65-074.1

Allard, J., Chaumillon, E., Féniès, H., 2009. A synthesis of morphological evolutions and Holocene stratigraphy of a wave-dominated estuary: The Arcachon lagoon, SW France. Continental Shelf Research 29, 957–969. https://doi.org/10.1016/j.csr.2008.11.017

Almar, R., Kestenare, E., Reyns, J., Jouanno, J., Anthony, E.J., Laibi, R., Hemer, M., Du Penhoat, Y., Ranasinghe, R., 2015. Response of the Bight of Benin (Gulf of Guinea, West Africa) coastline to anthropogenic and natural forcing, Part1: Wave climate variability and impacts on the longshore sediment transport. Continental Shelf Research 110, 48–59. https://doi.org/10.1016/j.csr.2015.09.020

Anderson, D., Ruggiero, P., Antolínez, J.A.A., Méndez, F.J., Allan, J., 2018. A Climate Index Optimized for Longshore Sediment Transport Reveals Interannual and Multidecadal Littoral Cell Rotations. Journal of Geophysical Research: Earth Surface. https://doi.org/10.1029/2018JF004689

Arnoux, F., Abadie, S., Bertin, X., Kojadinovic, I., 2018. A Database to Study Storm Impact Statistics along the Basque Coast. Journal of Coastal Research 85, 806–810. https://doi.org/10.2112/SI85-162.1

Barnard, P.L., Allan, J., Hansen, J.E., Kaminsky, G.M., Ruggiero, P., Doria, A., 2011. The impact of the 2009-10 El Niño Modoki on U.S. West Coast beaches. Geophysical Research Letters 38, n/a-n/a. https://doi.org/10.1029/2011GL047707

Battjes, J.A., Janssen, J.P.F.M., 1978. Energy Loss and Set-Up Due to Breaking of Random Waves, in: Coastal Engineering 1978. Presented at the 16th International Conference on Coastal Engineering, American Society of Civil Engineers, Hamburg, Germany, pp. 569–587. https://doi.org/10.1061/9780872621909.034

Bertin, X., Bruneau, N., Breilh, J.-F., Fortunato, A.B., Karpytchev, M., 2012. Importance of wave age and resonance in storm surges: The case Xynthia, Bay of Biscay. Ocean Modelling 42, 16–30. https://doi.org/10.1016/j.ocemod.2011.11.001

Bertin, X., Fortunato, A.B., Oliveira, A., 2009. A modeling-based analysis of processes driving wave-dominated inlets. Continental Shelf Research 29, 819–834. https://doi.org/10.1016/j.csr.2008.12.019

Bertin, X., Li, K., Roland, A., Bidlot, J.-R., 2015. The contribution of short-waves in storm surges: Two case studies in the Bay of Biscay. Continental Shelf Research 96, 1–15. https://doi.org/10.1016/j.csr.2015.01.005

Bertin, X., Mengual, B., de Bakker, A., Guérin, T., Martins, K., Pezert, M., Lavaud, L., 2020. Recent Advances in Tidal Inlet Morphodynamic Modelling. Journal of Coastal Research 95, 1016. https://doi.org/10.2112/SI95-198.1

Brakenhoff, L., Schrijvershof, R., van der Werf, J., Grasmeijer, B., Ruessink, G., van der Vegt, M., 2020. From Ripples to Large-Scale Sand Transport: The Effects of Bedform-Related Roughness on Hydrodynamics and Sediment Transport Patterns in Delft3D. JMSE 8, 892. https://doi.org/10.3390/jmse8110892

Bruneau, N., Bertin, X., Castelle, B., Bonneton, P., 2014. Tide-induced flow signature in rip currents on a meso-macrotidal beach. Ocean Modelling 74, 53–59. https://doi.org/10.1016/j.ocemod.2013.12.002

Bruneau, N., Fortunato, A.B., Dodet, G., Freire, P., Oliveira, A., Bertin, X., 2011. Future evolution of a tidal inlet due to changes in wave climate, Sea level and lagoon morphology (Óbidos lagoon,

573 Portugal). Continental Shelf Research 31, 1915–1930.
574 https://doi.org/10.1016/j.csr.2011.09.001
575 Camenen, B., Larson, M., 2007. A unified sediment transport formulation for inlet application (No.
576 ERDC/CHL CR-07-1). U.S. Army Engineer Research and Development Center, Vicksburg, MS.
577 Capo, S., Lubac, B., Marieu, V., Robinet, A., Bru, D., Bonneton, P., 2014. Assessment of the decadal
578 morphodynamic evolution of a mixed energy inlet using ocean color remote sensing. Ocean
579 Dynamics 64, 1517–1530. https://doi.org/10.1007/s10236-014-0762-1
580 Cayocca, F., 2001. Long-term morphological modeling of a tidal inlet: the Arcachon Basin, France.
581 Coastal Engineering 42, 115–142. https://doi.org/10.1016/S0378-3839(00)00053-3
582 Cayocca, F., 1996. Modélisation morphodynamique d'une embouchure tidale: application aux passes
583 d'entrée du Bassin d'Arcachon (Thèse de Doctorat). Université Bordeaux I.
584 Charles, E., Idier, D., Thiébot, J., Le Cozannet, G., Pedreros, R., Ardhuin, F., Planton, S., 2012. Present
585 Wave Climate in the Bay of Biscay: Spatiotemporal Variability and Trends from 1958 to 2001.
586 Journal of Climate 25, 2020–2039. https://doi.org/10.1175/JCLI-D-11-00086.1
587 Davis, R.A., FitzGerald, D.M., 2004. Tidal Inlets, in: Beaches and Coasts. Blackwell Science Ltd, pp.
588 209–244.
589 Demissie, H.K., Bacopoulos, P., 2017. Parameter estimation of anisotropic Manning's n coefficient for
590 advanced circulation (ADCIRC) modeling of estuarine river currents (lower St. Johns River).
591 Journal of Marine Systems 169, 1–10. https://doi.org/10.1016/j.jmarsys.2017.01.008
592 Doré, A., 2015. Modelling of the morphodynamic evolution of submarine sand dunes (Thèse de
593 Doctorat). Université de Bordeaux, Bordeaux, France.
594 Elias, E., Teske, R., Van Der Spek, A., Lazar, M., 2015. Modelling tidal-inlet morphodynamics on
595 medium time scales, in: Coastal Sediments 2015. WORLD SCIENTIFIC.
596 https://doi.org/10.1142/9789814689977_0230
597 Elias, E.P.L., Hansen, J.E., 2013. Understanding processes controlling sediment transports at the
598 mouth of a highly energetic inlet system (San Francisco Bay, CA). Marine Geology 345, 207–
599 220. https://doi.org/10.1016/j.margeo.2012.07.003
600 Elias, E.P.L., Van der Spek, A.J.F., Pearson, S.G., Cleveringa, J., 2019. Understanding sediment
601 bypassing processes through analysis of high-frequency observations of Ameland Inlet, the
602 Netherlands. Marine Geology 415, 105956. https://doi.org/10.1016/j.margeo.2019.06.001
603 Féniès, H., Lericolais, G., 2005. Internal architecture of an incised valley-fill on a wave- and tide-
604 dominated coast (the Leyre incised valley, Bay of Biscaye, France). Comptes Rendus
605 Geoscience 337, 1257–1266. https://doi.org/10.1016/j.crte.2005.06.005
606 Hansen, J.E., Elias, E., List, J.H., Erikson, L.H., Barnard, P.L., 2013. Tidally influenced alongshore
607 circulation at an inlet-adjacent shoreline. Continental Shelf Research 56, 26–38.
608 https://doi.org/10.1016/j.csr.2013.01.017
609 Hayes, M.O., 1979. Barrier island morphology as a function of tidal and wave regime, in: Barrier
610 Islands, from the Gulf of St. Lawrence to the Gulf of Mexico. Leatherman, S., pp. 1–27.
611 Herrling, G., Winter, C., 2018. Tidal inlet sediment bypassing at mixed-energy barrier islands. Coastal
612 Engineering 140, 342–354. https://doi.org/10.1016/j.coastaleng.2018.08.008
613 Hoan, L.X., Hanson, H., Larson, M., Kato, S., 2011. A mathematical model of spit growth and barrier
614 elongation: Application to Fire Island Inlet (USA) and Badreveln Spit (Sweden). Estuarine,
615 Coastal and Shelf Science 93, 468–477. https://doi.org/10.1016/j.ecss.2011.05.033
616 Hurrell, J.W., 2015. The Climate Data Guide: Hurrell North Atlantic Oscillation (NAO) Index (Station-
617 based).
618 Hurrell, J.W., Deser, C., 2009. North Atlantic climate variability: The role of the North Atlantic
619 Oscillation. Journal of Marine Systems 78, 28–41.
620 https://doi.org/10.1016/j.jmarsys.2008.11.026
621 Idier, D., Castelle, B., Charles, E., Mallet, C., 2013. Longshore sediment flux hindcast: spatio-temporal
622 variability along the SW Atlantic coast of France. Journal of Coastal Research 165, 1785–
623 1790. https://doi.org/10.2112/SI65-302.1

Kalnay, E., Kanamitsu, M., Kistler, R., Collins, W., Deaven, D., Gandin, L., Iredell, M., Saha, S., White, G., Woollen, J., Zhu, Y., Leetmaa, A., Reynolds, R., Chelliah, M., Ebisuzaki, W., Higgins, W., Janowiak, J., Mo, K.C., Ropelewski, C., Wang, J., Jenne, R., Joseph, D., 1996. The NCEP/NCAR 40-Year Reanalysis Project. Bulletin of the American Meteorological Society 77, 437–471. https://doi.org/10.1175/1520-0477(1996)077<0437:TNYRP>2.0.CO;2

Kraus, N.C., 2000. Reservoir Model of Ebb-Tidal Shoal Evolution and Sand Bypassing. Journal of Waterway, Port, Coastal, and Ocean Engineering 126, 305–313. https://doi.org/10.1061/(ASCE)0733-950X(2000)126:6(305)

Larson, M., Camenen, B., Nam, P.T., 2011. A Unified Sediment Transport Model for Inlet Application. Journal of Coastal Research 59, 27–38. https://doi.org/10.2112/SI59-004.1

Larson, M., Kraus, N.C., Connell, K.J., 2007. MODELING SEDIMENT STORAGE AND TRANSFER FOR SIMULATING REGIONAL COASTAL EVOLUTION, in: Coastal Engineering 2006. Presented at the Proceedings of the 30th International Conference, World Scientific Publishing Company, San Diego, California, USA, pp. 3924–3936. https://doi.org/10.1142/9789812709554_0330

Lenstra, K.J.H., Ridderinkhof, W., Vegt, M., 2019. Unraveling the Mechanisms That Cause Cyclic Channel-Shoal Dynamics of Ebb-Tidal Deltas: A Numerical Modeling Study. J. Geophys. Res. Earth Surf. 124, 2778–2797. https://doi.org/10.1029/2019JF005090

Marchesiello, P., Kestenare, E., Almar, R., Boucharel, J., Nguyen, N.M., 2020. Longshore drift produced by climate-modulated monsoons and typhoons in the South China Sea. Journal of Marine Systems 211, 103399. https://doi.org/10.1016/j.jmarsys.2020.103399

Meistrell, F.J., 1972. The spit-platform concept: laboratory observation of spit development, in: Schwartz, M.L. (Ed.), Spits and Bars. Dowden, Hutchinson & Ross, pp. 225–283.

Mugica, J., Paris, F., Nicolae Lerma, A., Pedreros, R., Ayache, B., Garcin, M., Bulteau, T., Hoareau, A., 2016. Caractérisation de l'aléa submersion marine dans le cadre des PPRL du Bassin d'Arcachon - Approche dynamique avec prise en compte des ouvrages de protection côtière. Rapport final. (No. BRGM/RP-64807-FR). BRGM, Orléans, France.

Nahon, A., 2018. Ongoing morphological evolution of a Holocene coastal barrier spit - The Cap Ferret, at the entrance of the Bay of Arcachon (PhD Thesis). University of Bordeaux, Bordeaux, France.

Nahon, A., Idier, D., Sénéchal, N., Féniès, H., Mallet, C., Mugica, J., 2019. Imprints of wave climate and mean sea level variations in the dynamics of a coastal spit over the last 250 years: Cap Ferret, SW France. Earth Surface Processes and Landforms esp.4634. https://doi.org/10.1002/esp.4634

Nichols, M., Allen, G., 1981. Sedimentary processes in coastal lagoons. Unesco Technical Papers In Marine Science 27–80.

Nienhuis, J.H., Ashton, A.D., 2016. Mechanics and rates of tidal inlet migration: modeling and application to natural examples: InletMigration. Journal of Geophysical Research: Earth Surface. https://doi.org/10.1002/2016JF004035

Nienhuis, J.H., Lorenzo-Trueba, J., 2019. Can Barrier Islands Survive Sea-Level Rise? Quantifying the Relative Role of Tidal Inlets and Overwash Deposition. Geophys. Res. Lett. 46, 14613–14621. https://doi.org/10.1029/2019GL085524

Oertel, G.F., 1985. The barrier island system. Marine Geology 63, 1–18. https://doi.org/10.1016/0025-3227(85)90077-5

Orescanin, M.M., Elgar, S., Raubenheimer, B., 2016. Changes in bay circulation in an evolving multiple inlet system. Continental Shelf Research 124, 13–22. https://doi.org/10.1016/j.csr.2016.05.005

Poirier, C., Tessier, B., Chaumillon, É., Bertin, X., Fruergaard, M., Mouazé, D., Noël, S., Weill, P., Wöppelmann, G., 2017. Decadal changes in North Atlantic atmospheric circulation patterns recorded by sand spits since 1800CE. Geomorphology 281, 1–12. https://doi.org/10.1016/j.geomorph.2016.12.028

Ridderinkhof, W., de Swart, H.E., van der Vegt, M., Hoekstra, P., 2016. Modeling the growth and migration of sandy shoals on ebb-tidal deltas. Journal of Geophysical Research: Earth Surface. https://doi.org/10.1002/2016JF003823

Roland, A., Zhang, Y.J., Wang, H.V., Meng, Y., Teng, Y.-C., Maderich, V., Brovchenko, I., Dutour-Sikiric, M., Zanke, U., 2012. A fully coupled 3D wave-current interaction model on unstructured grids. Journal of Geophysical Research: Oceans 117, n/a-n/a. https://doi.org/10.1029/2012JC007952

Senechal, N., Sottolichio, A., Bertrand, F., Goeldner-Gianella, L., Garlan, T., 2013. Observations of waves' impact on currents in a mixed-energy tidal inlet: Arcachon on the southern French Atlantic coast. Journal of Coastal Research 165, 2053–2058. https://doi.org/10.2112/SI65-347.1

SHOM, 2014. Références altimétriques maritimes - édition 2014.

SHOM, n.d. Tide gauge Arcachon Eyrac [WWW Document]. URL https://data.shom.fr/donnees/refmar/190 (accessed 14/05/2020).

Silva, A.P., Klein, A.H.F., Fetter-Filho, A.F.H., Hein, C.J., Méndez, F.J., Broggio, M.F., Dalinghaus, C., 2020. Climate-induced variability in South Atlantic wave direction over the past three millennia. Sci Rep 10, 18553. https://doi.org/10.1038/s41598-020-75265-5

Smith, J.M., Larson, M., Kraus, N.C., 1993. Longshore current on a barred beach: Field measurements and calculation. Journal of Geophysical Research 98, 22717. https://doi.org/10.1029/93JC02116

Soulsby, R., 1997. Dynamics of Marine Sands. Thomas Telford Ltd. https://doi.org/10.1680/doms.25844

Splinter, K.D., Davidson, M.A., Golshani, A., Tomlinson, R., 2012. Climate controls on longshore sediment transport. Continental Shelf Research 48, 146–156. https://doi.org/10.1016/j.csr.2012.07.018

Teske, R., 2013. Tidal inlet channel stability in long term process based modelling (MSc Thesis). Utrecht University.

van Ormondt, M., Nelson, T.R., Hapke, C.J., Roelvink, D., 2020. Morphodynamic modelling of the wilderness breach, Fire Island, New York. Part I: Model set-up and validation. Coastal Engineering 157, 103621. https://doi.org/10.1016/j.coastaleng.2019.103621

van Rijn, L.C., 2007. Unified View of Sediment Transport by Currents and Waves. I: Initiation of Motion, Bed Roughness, and Bed-Load Transport. Journal of Hydraulic Engineering 133, 649–667. https://doi.org/10.1061/(ASCE)0733-9429(2007)133:6(649)

Vaucher, R., Pittet, B., Humbert, T., Ferry, S., 2018. Large-scale bedforms induced by supercritical flows and wave–wave interference in the intertidal zone (Cap Ferret, France). Geo-Mar Lett 38, 287–305. https://doi.org/10.1007/s00367-017-0526-2

Walton, Jr., T.L., Adams, W.D., 1976. Capacity of inlet outer bars to store sand, in: Proceedings of the 15th Coastal Engineering Conference, Honolulu, HI. ASCE, pp. 1919–1937.

Wiggins, M., Scott, T., Masselink, G., McCarroll, R.J., Russell, P., 2020. Predicting beach rotation using multiple atmospheric indices. Marine Geology 426, 106207. https://doi.org/10.1016/j.margeo.2020.106207

Zhang, Y.J., Ye, F., Stanev, E.V., Grashorn, S., 2016. Seamless cross-scale modeling with SCHISM. Ocean Modelling 102, 64–81. https://doi.org/10.1016/j.ocemod.2016.05.002

719 **Table 1** – Comparison of modelled and observed elevations at locations A, B and C shown on Figure
720 1; a_{M2} and a_{M4} are the amplitude of tidal component M2 and M4 respectively and θ_{M2} and θ_{M4} their
721 respective phase (adapted from Nahon, 2018).

	Bias (cm)	Erms (cm)	a_{M2} (m)	a_{M4} (m)	θ_{M2} (°)	θ_{M4} (°)	a_{M4}/a_{M2}	$2\theta_{M2} - \theta_{M4}$
Obs. A	--	--	1.36	0.05	93.1	322.0	0.035	224.4
Mod. A	-0.21	7.35	1.36	0.04	91.5	324.0	0.029	219.0
Obs. B	--	--	1.45	0.03	105.0	30.3	0.019	179.7
Mod. B	2.25	10.39	1.42	0.07	105.0	57.1	0.049	152.9
Obs. C	--	--	1.36	0.08	121.0	35.6	0.061	206.4
Mod. C	-1.93	11.84	1.35	0.11	116.0	26.6	0.078	205.0

722

723 **Table 2** – Tidal (M2) amplitude, mean wave parameters and estimated transport and sedimentation
724 rates near the spit's distal end for 8 selected simulations; LST values correspond to the average
725 southward transport in cells 5 to 10 (dashed black frames on **Figure 5** and **6**); ΔVw and ΔVs are the
726 average estimated volumetric changes (per 300-m wide cell) in the western and southern groups,
727 respectively.

Simulations	M2 (m)	Hs (m)	Tp (s)	Dir (°)	LST (10^3 $m^3.y^{-1}$)	ΔVw (10^3 $m^3.y^{-1}$)	ΔVs (10^3 $m^3.y^{-1}$)	Platform (10^3 $m^3.y^{-1}$)
SIM1	3.6	0.00	0.00	-	1.1	6	16	-
SIM2	0.0	2.02	11.79	291.83	150.2	186	-95	-
SIM3	3.6	2.02	11.79	291.83	166.5	-51	-312	644
SIM4	3.6	2.56	13.00	290.00	304.2	-6	-329	705
SIM5	3.6	2.41	13.00	290.00	258.5	-17	-328	676
SIM6	3.6	2.70	13.00	290.00	357.2	8	-335	763
SIM7	3.6	2.56	13.00	286.00	205.0	-15	-311	648
SIM8	3.6	2.56	13.00	294.00	411.1	3	-347	819

728

729

730 **Table 3** – Tidal (M2) amplitude and mean wave parameters for 9 sensitivity analysis simulations, in
731 bold are indicated changes from simulations given in **Table 2;** LST values are the same as in **Table 2**.

Simulations	M2 (m)	Hs (m)	Tp (s)	Dir (°)	LST (10^3 $m^3.y^{-1}$)	other
SIM3a	3.6	2.02	11.79	291.83	379.1	**Manning's n = 0.02 $s/m^{1/3}$**
SIM3b	3.6	2.02	11.79	291.83	145.5	**Bedforms (RS97)**
SIM3c	3.6	2.02	11.79	291.83	461.8	**Bedforms (VR07)**
SIM3d	3.6	2.02	11.79	291.83	411.8	**$0.019 \leq n \leq 0.040$ $s/m^{1/3}$**
SIM4a	**1.8**	2.56	13.00	290.00	291.4	
SIM7a	**1.8**	2.56	13.00	286.00	185.9	
SIM8a	**1.8**	2.56	13.00	294.00	397.9	
SIM4b	**4.5**	2.56	13.00	290.00	316.2	
SIM7b	**4.5**	2.56	13.00	286.00	219.8	
SIM8b	**4.5**	2.56	13.00	294.00	420.9	

732

733

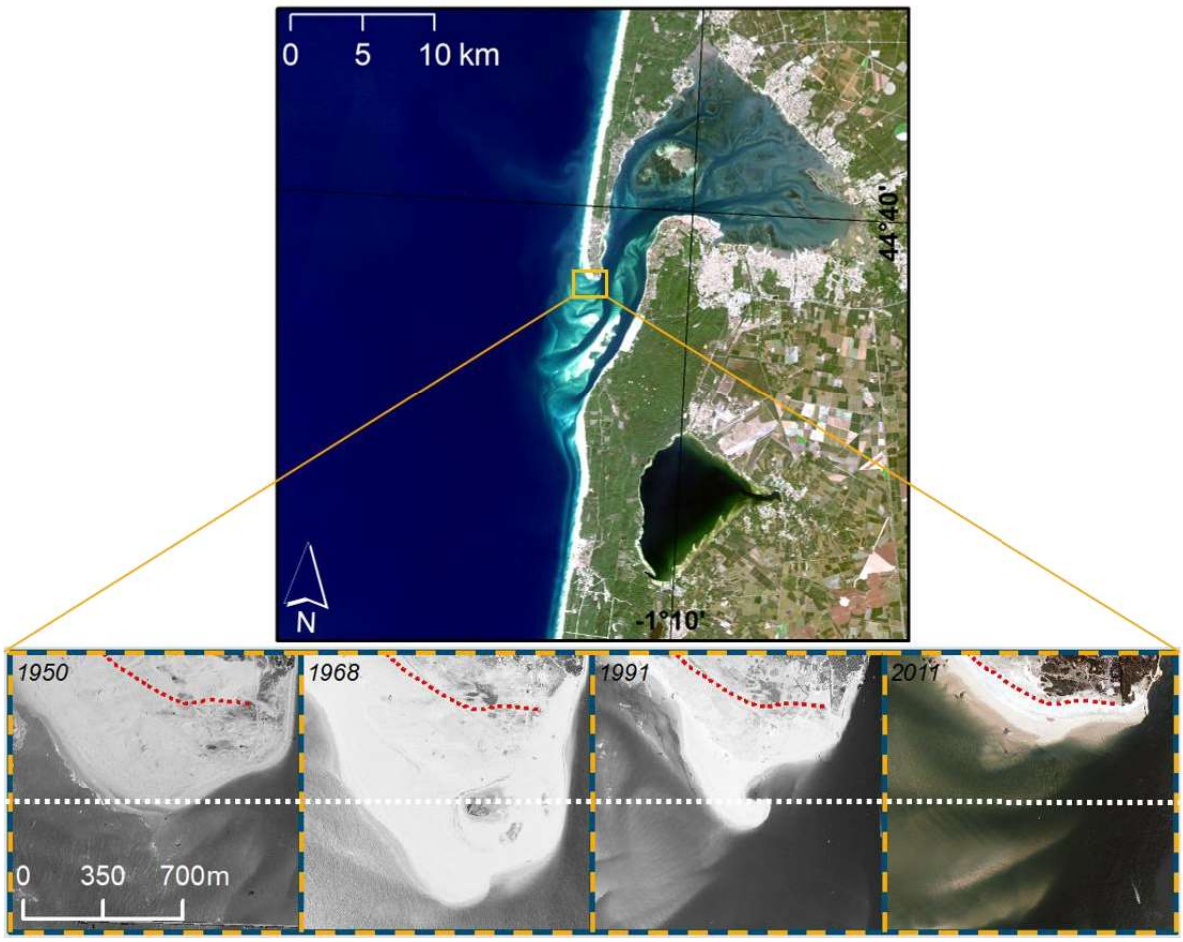

734

735 **Figure 1 –** Satellite view of the Bay of Arcachon (Landsat 8, October 2014), with aerial photos of Cap
736 Ferret's distal end from 1950 to 2011 (red dotted line indicates the position of the dune toe in
737 October 2014).

738

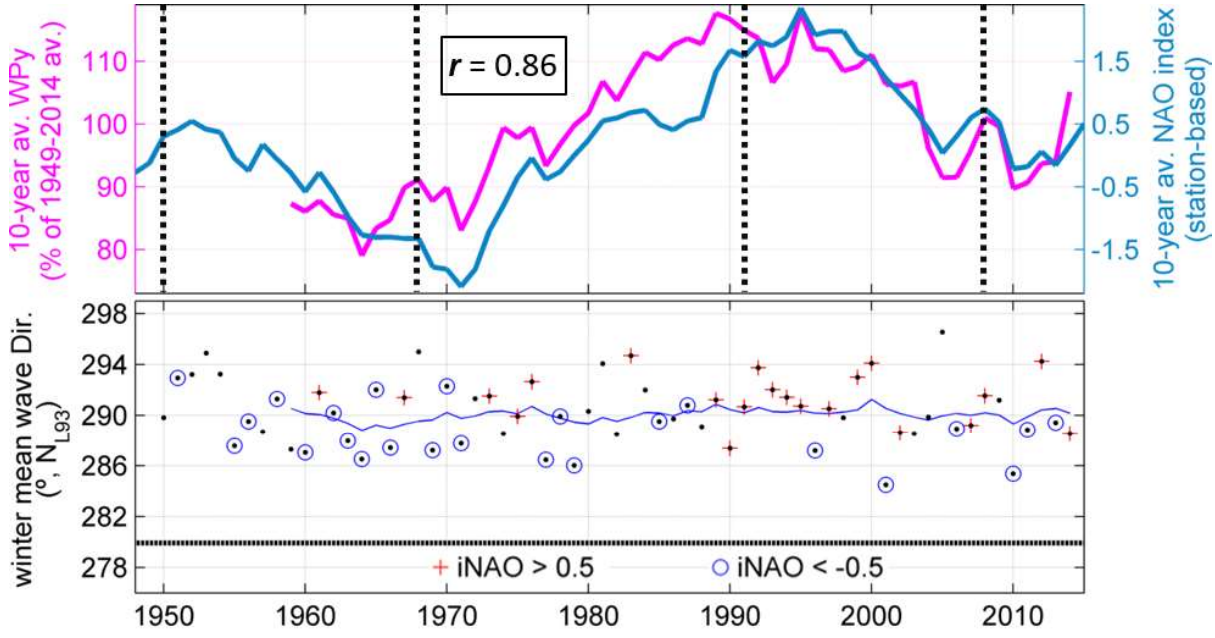

739

740 **Figure 2 –** Winter -DJFM- wave climate. **Upper panel**: decadal average of the normalized longshore
741 wave power (WPy) and of the NAO station-based index (running mean of the winter averaged values,
742 decentred over the ten preceding years), vertical dotted lines stand for the date of the photos on
743 **Figure 1**, ***r*** is Pearson's linear correlation coefficient between the two curves; **lower panel**: direction
744 of winter mean incident wave power, expressed in nautical convention into Lambert-93 projection
745 (subtract 3.12˚ for true north), the thin blue line is the decadal average and the dotted black line is
746 the direction normal to the 20-km spit orientation.

747

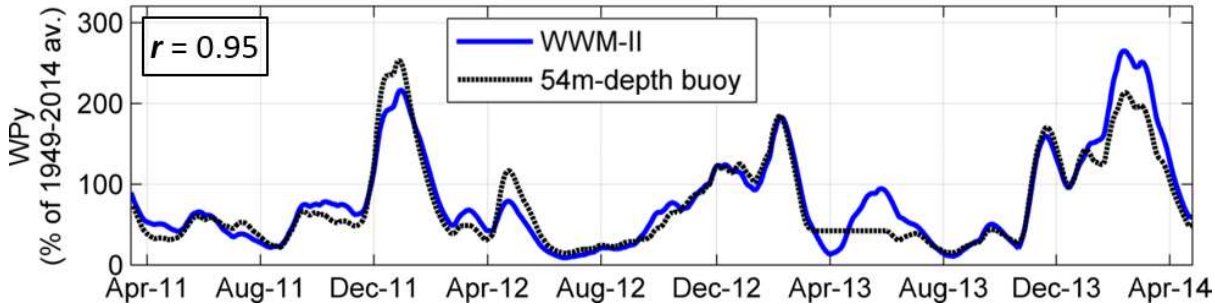

748

749 **Figure 3 –** Comparison of hindcasted (solid blue curve) and observed (dotted black curve) normalized
750 longshore wave power (WPy), 90-day centred average, ***r*** is Pearson's linear correlation coefficient
751 between the two curves.

752

753

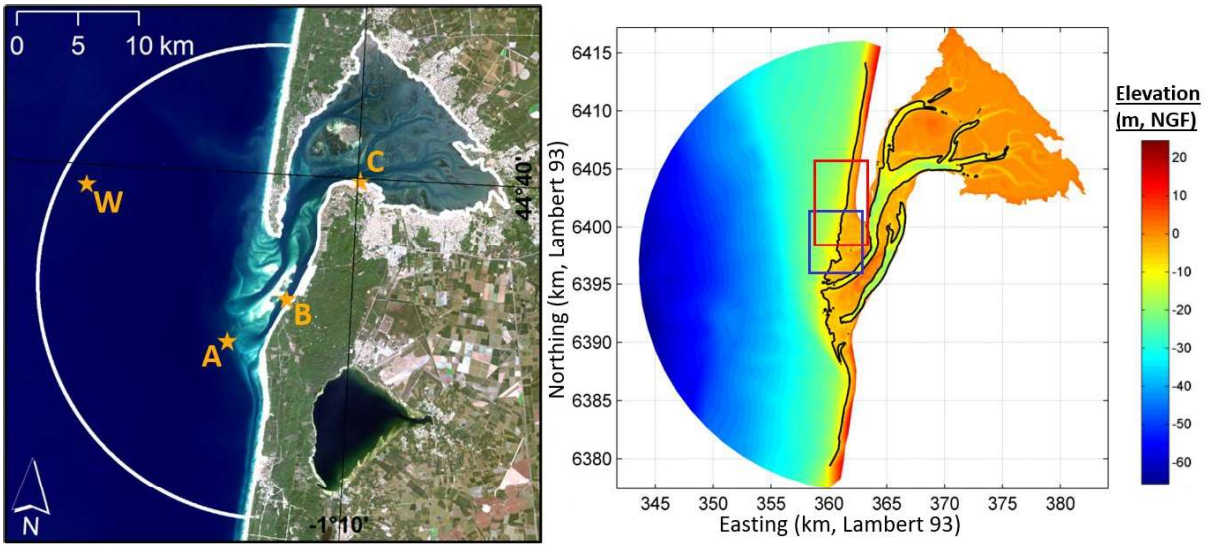

Figure 4 – Model domain. **Left panel**: satellite Landsat 8 view of the Bay of Arcachon and its tidal inlet on October 1st, 2014, the white contour represents the boundary of SCHISM's computational grid and the four yellow stars stand for the Cap Ferret wave buoy (W), the ebb-tidal delta pressure sensor (A), the southern channel pressure sensor (B) and *Eyrac*'s tide gauge (C); **right panel**: model computational domain and bathymetry (local mean sea level is at +0.36 m NGF), black contours correspond to -7 m NGF, the red frame shows the area of interest at the distal end of Cap Ferret and corresponds to **Figure 5** extent, the blue frame is the area over which the spit platform sedimentation rate was computed.

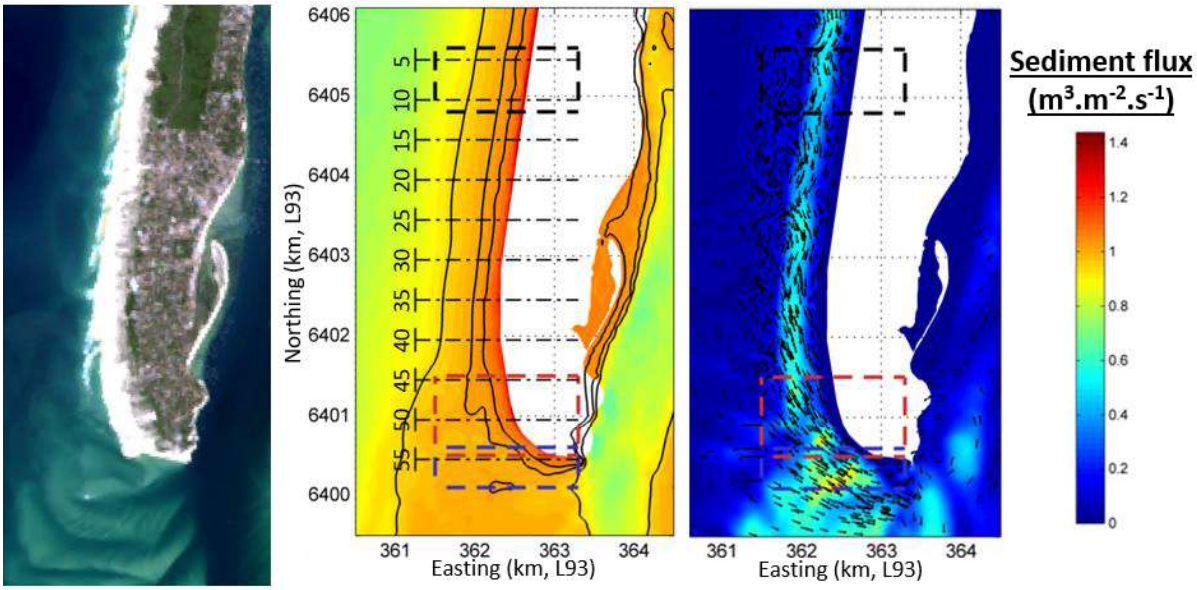

764

765 **Figure 5** – Modelling sediment transport patterns at the distal end of Cap Ferret. **Left panel:** Satellite
766 Landsat 8 view of the subaerial spit's last 5 km on October 1st, 2014; **centre panel:** model
767 bathymetry, solid black lines stand for the -7 m NGF, -2 m NGF and 0 m NGF contours (-2 m is close
768 to the offshore limit of the intertidal area), dashed frames delimit sediment transport integration
769 cells highlighted in **Figures 6-9 & 14**, with in red the western group and in blue the southern group,
770 the dot-dashed lines stand for the centres of cell number 5 to 55 with the vertical standing for the
771 cells' width; **right panel:** residual sediment transport patterns in the average winter case (SIM4).

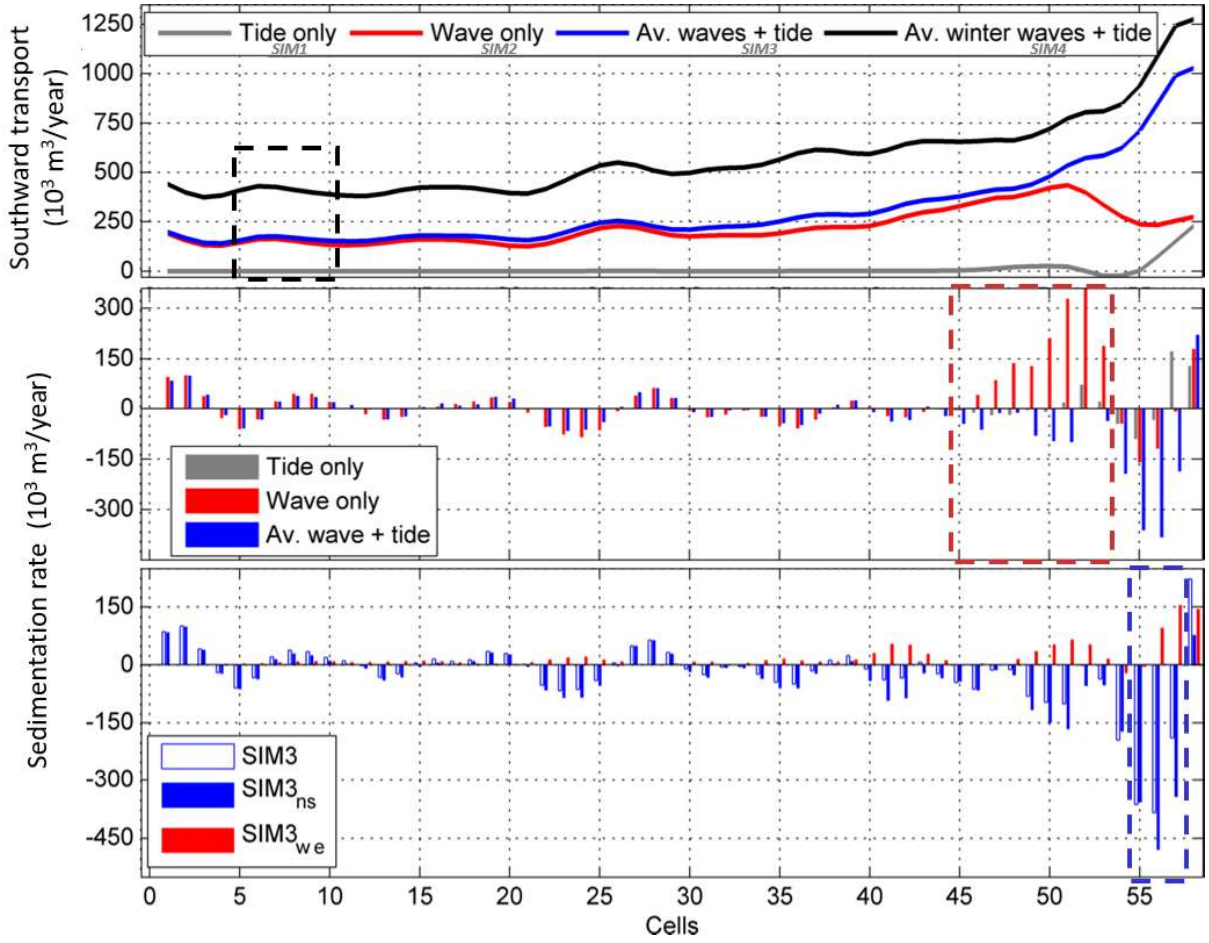

772

773 **Figure 6 –** Integrated sediment transport patterns. **Upper panel:** cell-averaged southward sediment
774 transport, integrated in the west-east direction (SIM1 to SIM4); **centre panel:** cell-integrated
775 sedimentation rates for SIM1 to SIM3; **lower panel:** cell-integrated sedimentation rates for SIM3,
776 with the respective contributions of the southward (ns) and eastward (we) transport components.
777 Simulation names refer to simulation parameters given in **Table 2** and the dashed framed cells
778 correspond to delimited areas on **Figure 5** centre panel.

779

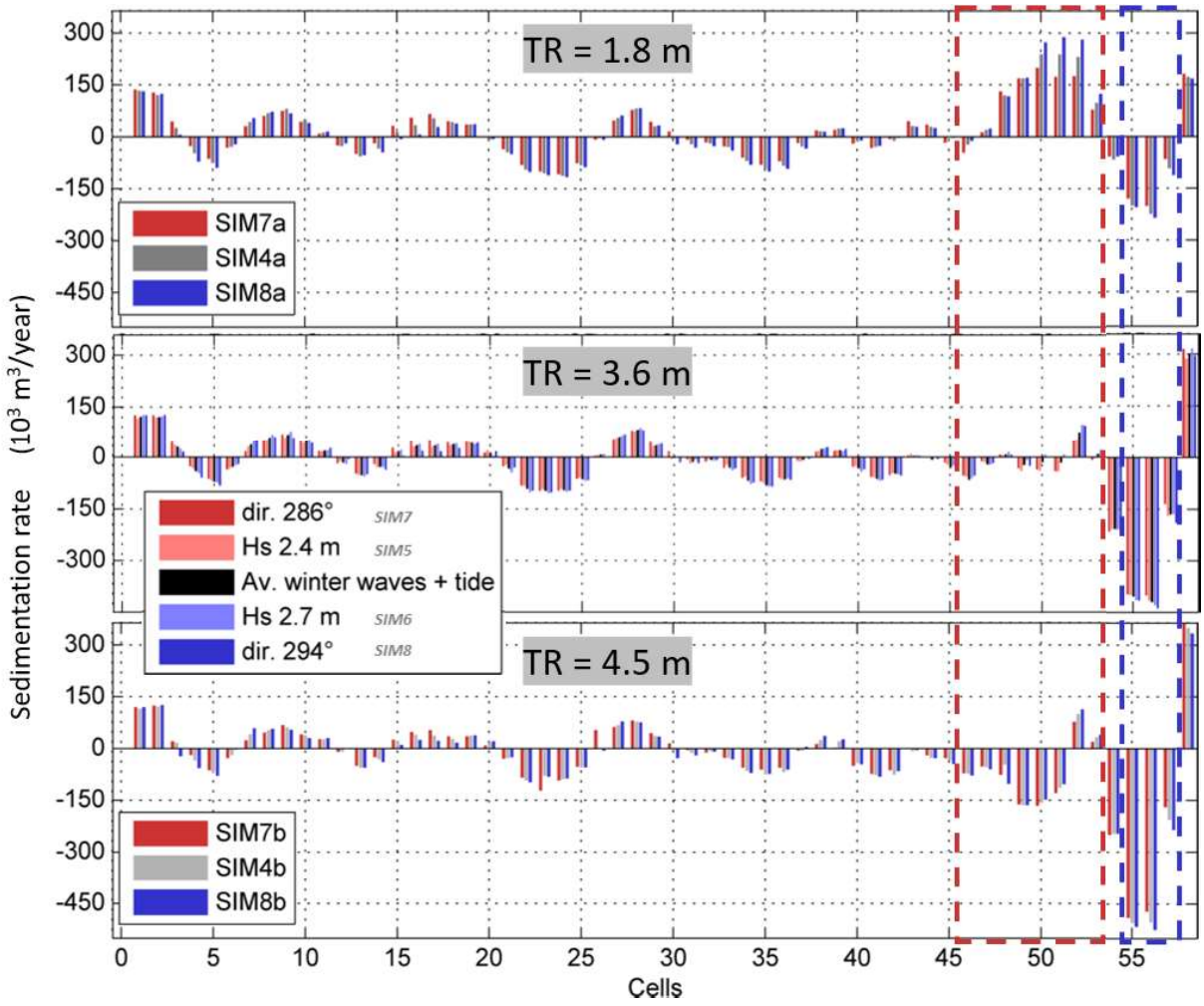

780

781 **Figure 7 –** Cell-integrated sedimentation rates for winter wave climate scenarios and for three
782 different values of tidal range (TR). Simulation names refer to simulation parameters given in **Table 2**
783 and **Table 3,** and the dashed framed cells correspond to delimited areas on **Figure 5** centre panel.

784

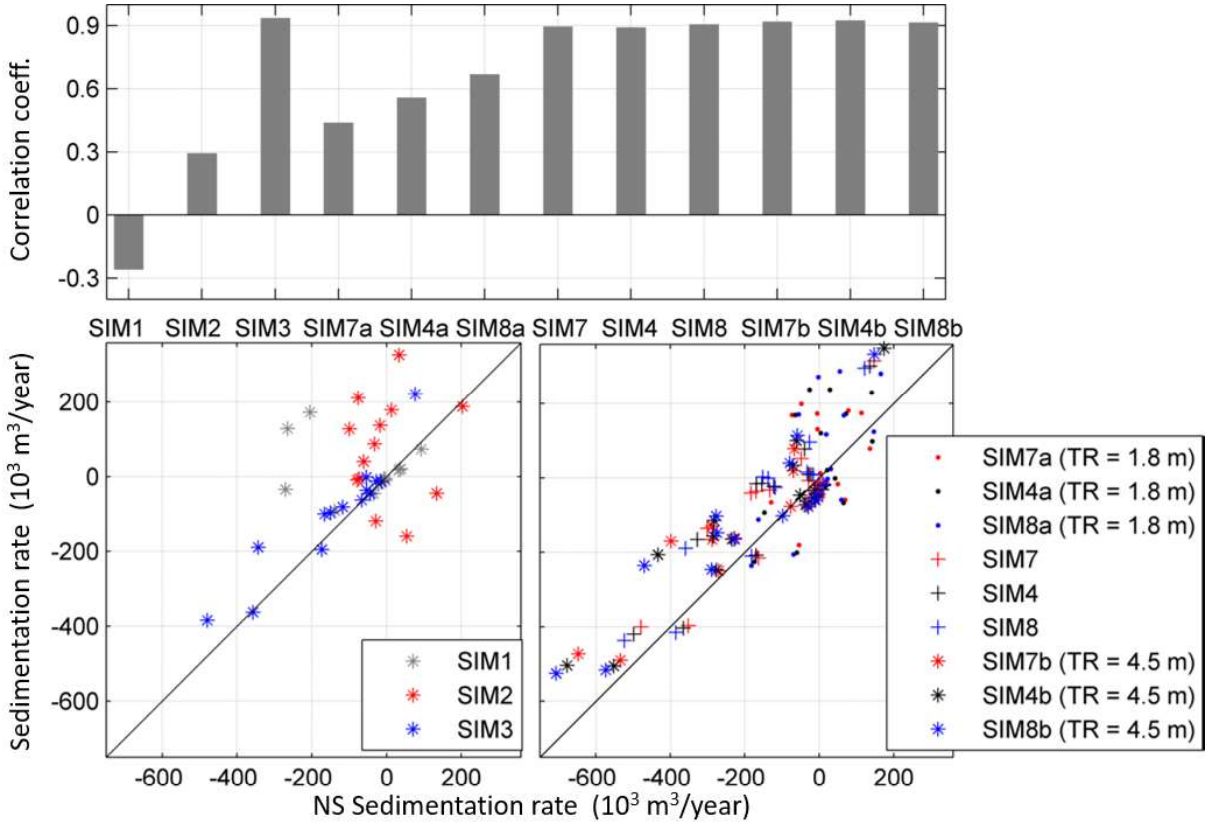

785

786 **Figure 8 –** Total sedimentation rate *vs.* sedimentation associated with south-north sediment fluxes
787 from cell number 45 to cell number 58. U**pper panel:** Pearson's linear correlation coefficients
788 between both cell-averaged sedimentation rates; **lower panel**s: scatter plot of this quantities, with
789 the black straight curve standing for equation y = x. Simulation names refer to simulation parameters
790 given in **Table 2** and **Table 3**.

791

792

793

794

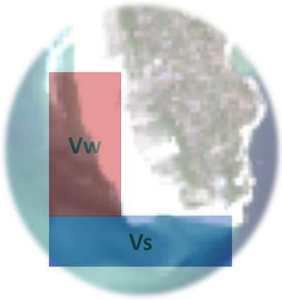

Representative conditions

	ΔVw	ΔVs
Tide only	0.10	0.05
Wave only	3.66	-0.29
Wave + tide	**-1.00**	-0.95

Winter representtive conditions

	ΔVw	ΔVs
NAO **– ; -4º**	-0.33 ; -0.31	-0.99 ; -0.94
Average	-0.11	**-1.00**
NAO **+ ; +4º**	0.16 ; 0.06	-1.02 ; -1.05

Figure 9 – Normalized averaged volumetric variations per cell in the western (ΔVw) and southern (ΔVs) group of cells indicated in **Figure 5**, for annual representative wave climate and winter representative wave climates associated with the dominant phase of the NAO. Positive values in red stand for accretion while negative value in blue stand for erosion, ΔVw values were normalized by SIM3 (waves and tide) absolute value while ΔVs were normalized by the one of SIM4 (winter waves and tide)

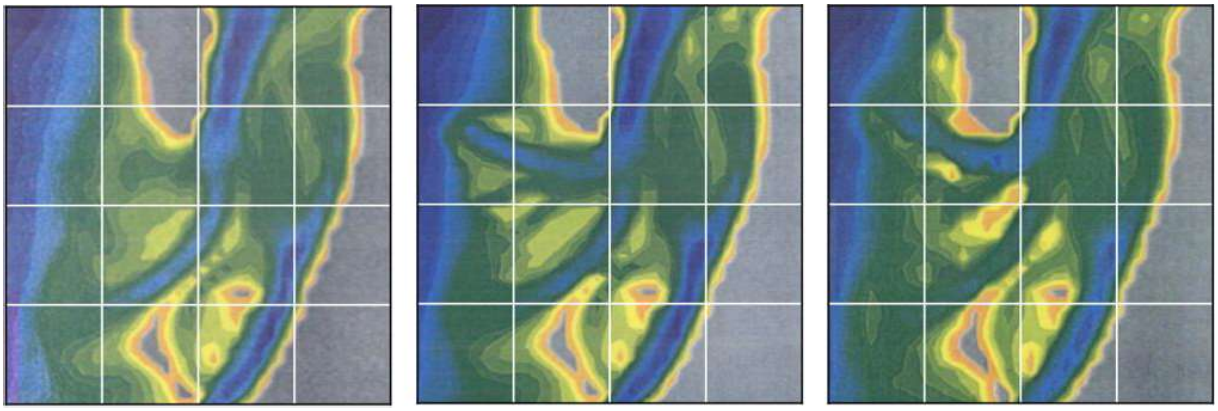

Figure 10 – Morphodynamic results of Cayocca (2001, 1996), adapted from Cayocca (1996). **Left panel:** initial model bathymetry contours, from -20.8 m NGF (dark blue shade) to +2 m NGF (grey shade) at 1.2 m interval; **centre panel:** simulated morphology after 50 morphological timesteps with tidal forcing only; **right panel:** simulated morphology after 50 morphological timesteps with tidal and wave forcing.

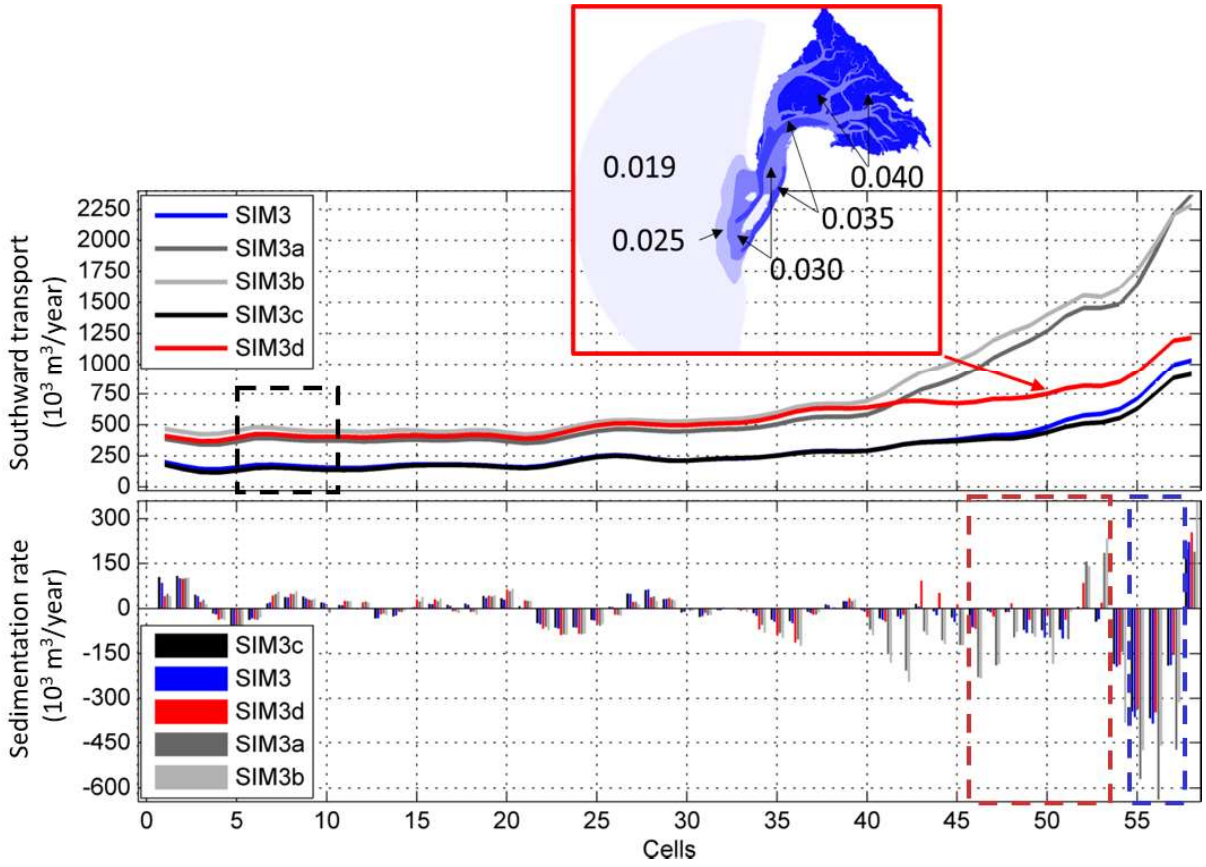

809

810 **Figure 11 –** Sensitivity of integrated sediment transport patterns to spatio-temporally varying bottom
811 friction coefficient (SIM3a-d). **Upper panel:** cell-averaged southward sediment transport, integrated
812 in the west-east direction; **lower panel:** cell-integrated sedimentation rates; **red inset:** spatial
813 repartition of the Manning coefficient ($s/m^{1/3}$) used in SIM3d, adapted from Mugica et al. (2016).
814 Simulation names refer to simulation parameters given in **Table 2** and **Table 3**, and dashed framed
815 cells correspond to delimited areas on **Figure 5** centre panel.

Declaration of interests

☒ The authors declare that they have no known competing financial interests or personal relationships that could have appeared to influence the work reported in this paper.

☐The authors declare the following financial interests/personal relationships which may be considered as potential competing interests: